Mechanisms of surface solar irradiance variability under broken clouds

Wouter Mol[1] and Chiel van Heerwaarden[1]

[1]Meteorology & Air Quality, Wageningen University

Correspondence: Wouter Mol (wbmol@wur.nl)

Abstract. Surface solar irradiance variability is present under all broken clouds, but the patterns, magnitude of variability, and mechanisms behind it vary greatly with cloud type. In this study, we performed numerical experiments to understand which main mechanisms drive surface solar irradiance extremes across a diverse set of cloud conditions based on observations. The results show that we can capture the essence in four mechanisms. We find that for optically thin ($\tau < 6$) and clouds, scattering in the forward direction (*forward escape*) is the dominant mechanism. In cloud types such as altocumulus, it is able to produce irradiance enhancements of up to 50 % of clear-sky values due to small gaps in the cloud field. For flat, optically thick clouds ($\tau > 6$) like stratus, *downward escape* becomes the dominant mechanism, and the irradiance extremes are found underneath the cloud edge or gaps. Albedo has a significant effect under optically thick cloud cover, contributing 10 to 60 % of the total irradiance enhancement for low (0.2) to high (0.8) albedo. For deep convective clouds, *side escape* is the dominant mechanism enhancing domain-averaged diffuse irradiance. This effect has a large area of influence, extending over 20 km from the sunlit side of the cloud. Extreme irradiance enhancement, however, comes from *downward escape* and *forward escape* just underneath the cloud edge on the sunlit side, not from *side escape*. These results provide a framework for understanding the vast diversity and complexity found in surface solar irradiance and cloudiness. A next step is to apply this analysis to multi-layered cloud fields and non-isolated deep convective clouds.

1 Introduction

In this chapter, we aim to determine the main mechanisms that drive the spatial and temporal patterns of surface solar irradiance in the presence of clouds that we have observed throughout the work in this thesis. The motivation for this is to understand how different clouds and cloud fields create irradiance variability, which should help to simplify the vast diversity and complexity found in surface irradiance and cloudiness. In this introduction, we will first define what we mean by variability in surface solar irradiance (SSI) and demonstrate this with a diverse selection of (extreme) SSI variability from observations. This selection consists of prototype examples based on the 1 Hz BSRN data of Mol et al. (2023b) or on 1-minute data of the Veenkampen station (https://maq-observations.nl/veenkampen/). Additionally, we include a selection of spatially observed SSI extremes from the fieldwork described in Mol et al. (2024).

Then, we formulate our hypothesis that SSI variability can be explained by four mechanisms. These mechanisms are based on prior research and theory (Section 1.2). From the prototype examples we design idealised numerical experiments, both to

qualitatively reproduce the set of examples of observations, and demonstrate how the four mechanisms work and when they are effective. Once the basics are established, we introduce more realistically simulated cloud fields to see how the hypothesis holds up when the complexity of clouds and cloud fields increases. The tools we use to simulate the cloud fields and calculate radiative transfer are introduced in Section 2, followed by an overview of all experiments in Section 3.

1.1 Conditions of extreme variability

30

SSI variability at cloud-scale expresses itself in diverse ways, as will be shown shortly, and the choice of any definition is subjective and perhaps arbitrary. Here, we focus on conditions in which SSI is able to exceed clear-sky SSI, referred to as cloud-induced irradiance enhancement, or *irradiance enhancement* (IE). We further characterise SSI variability by having frequent and rapid fluctuations between (partial) shading and IE of at least 10 %, spatiotemporal SSI patterns with IE and shading in excess of minutes or kilometres, or simply by a single, large peak in SSI (IE > 30 %). This loose definition purposefully excludes some common but less pronounced SSI variability conditions, as the impact is lower, and we assume conditions are easier to understand when SSI variability is more pronounced. Furthermore, we will mostly present SSI normalised with clear-sky SSI to be able to compare across cases with varying solar zenith angles. As small absolute changes in SSI can result in relatively large irradiance enhancement at high solar zenith angles, we only consider solar zenith angles of 75° or below.

35
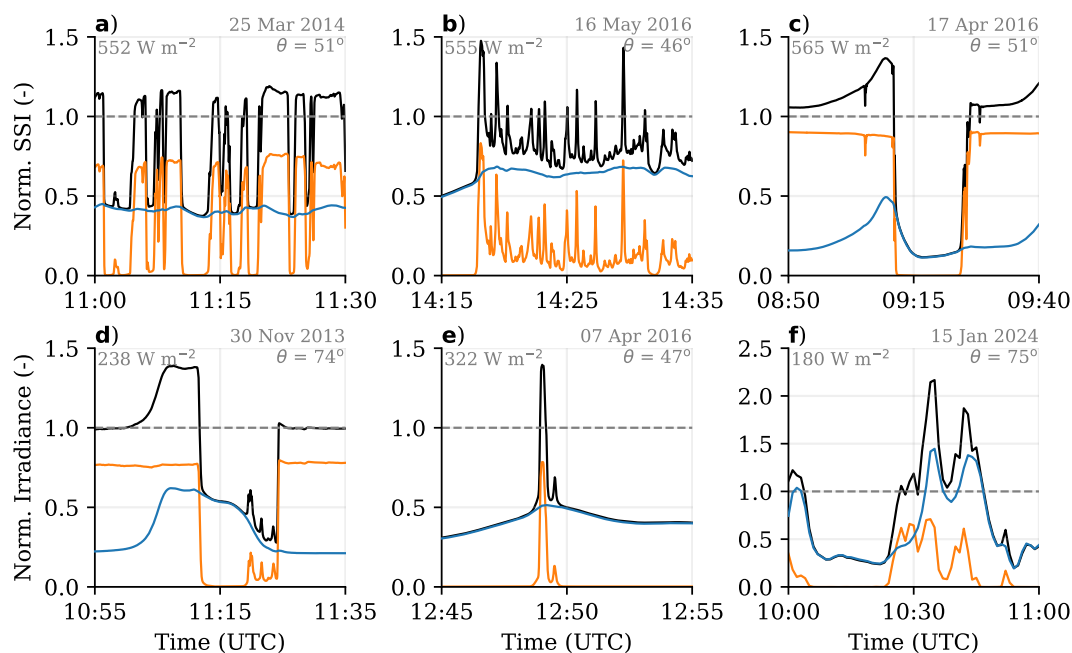
Figure 1. A collection of observed time series featuring irradiance variability under different conditions. The conditions are **(a)** shallow cumulus, **(b)** altocumulus, **(c)** cumulonimbus, **(d)** stratus field passage, **(e)** gap in stratocumulus, and **(f)** convective snow shower passage. All data is normalised with clear-sky SSI based on CAMS McClear (Gschwind et al., 2019). Average clear-sky SSI, solar zenith angle, and date are given in grey in the top of each subplot. Note that **(f)** has a larger y-axis.

1.1.1 Shallow cumulus

40 The shortwave radiative effects of shallow cumulus are the best described and studied among cloud types in the field of solar irradiance variability research. Key features are the fast and frequent transitions between shade and sunshine (Figure 1a), and the bimodal distribution of global horizontal irradiance (e.g., Gristey et al., 2020; Tijhuis et al., 2023). In the distribution, one peak is centred around the typical value of diffuse irradiance in cloud shadows where no direct irradiance is able to penetrate,

45 the other peak resembles the irradiance enhancement in directly sunlit areas. The shadows are typically dark and the transitions to sunlit areas are sharp, illustrated by examples of spatial SSI patterns of cumulus in Figure 2.

1.1.2 Altocumulus

Altocumulus cloud fields result in a bimodal SSI distribution too, but increased cloud cover fraction reduces how frequently irradiance enhancement occurs. Diffuse irradiance is generally higher than seen in most other conditions of SSI variability

50 and remains relatively constant on the spatiotemporal scale of individual irradiance enhancement peaks. Direct irradiance is often not completely attenuated, meaning the clouds are optically thin. Brief openings between individual altocumuli allow for direct irradiance to fully pass through and combine with the enhanced diffuse irradiance at the surface, thereby producing some of the most extreme observed IE peaks. Figure 1b shows all of these features in a time series, with one peak reaching nearly 50 % above clear-sky SSI. Fields of altocumuli were frequently observed while we did spatial SSI measurements during

55 the FESSTVaL campaign (Mol et al. (2024)). Figure 2 shows five different SSI patterns as a result of altocumulus, and one that includes cumulus as well. Peak irradiance enhancement varies between 30 and 60 % in these patterns. There are not many studies on altocumulus, but at least Schade et al. (2007) and Yordanov et al. (2015) also identified specifically altocumulus as being highly potent in creating such significant irradiance enhancement.

1.1.3 Cumulonimbus

60 Deep convective clouds with a vertically developed structure and anvil at the tropopause have the largest area of influence of the cloud types we consider in this study. The sheer size and scattering surface area of a single cumulonimbus cloud make it an ideal candidate for casting long shadows and enhancing diffuse irradiance on the sunlit side. Segal and Davis (1992) identified some of these features in observations, in particular the long-lasting irradiance enhancement at the sunlit side of the cumulonimbus clouds. Figure 1c shows the passage of a relatively isolated cumulonimbus moving from north to south over the

65 sensor location with the Sun in the south, from our own observations. The key SSI pattern features for this cloud-type are the slow ramping up of SSI on the sunlit side of the vertically developed cloud, subsequent rapid reduction to SSI values below even clear-sky diffuse irradiance, and the return to clear-sky SSI after the Sun reappears. In the observational example, this pattern is superimposed on a 5 % background enhancement of SSI that likely arises from other clouds in the vicinity. A fast rising cloud top of a cumulus congestus caused the shadow in the bottom right pattern of Figure 2, which is similar to the

70 reappearance part in the time series pattern.

1.1.4 Stratus and stratocumulus

Stratus and stratocumulus are generally optically thick cloud types that result in little SSI variability, unless they dissolve (or form), have gaps in them, or otherwise advect into or away from clear-sky region. Irradiance enhancement is not commonly associated with these cloud types, because the areas in which such variability can occur is small compared to the total cloud size, or brief compared to the total cloud lifetime. However, clear-sky to overcast conditions, or cloud gaps within overcast cloud fields, are associated with extreme irradiance peaks. Example are respectively illustrated in Figures 1d and 1e, and specifically for the cloud gap case in the study of Yordanov (2015). There is also a spatial SSI pattern caused by a small cumulus that formed in a cloud gap shown in the top left of Figure 2.

1.1.5 High albedo with broken cloud cover

A high albedo can enhance cloud-induced SSI variability by a significant amount, sometimes leading to extreme irradiance enhancement beyond what is normally observed under broken cloud cover. In Figure 1f, we show an example of a convective snow shower bringing a fresh layer of snow cover, which pushed the diffuse irradiance above clear-sky SSI values for multiple minutes. Such a measurement seems unrealistic, but has been observed before, see for example Gueymard (2017), their Figure 4. Villefranque et al. (2023) furthermore identified that surface albedo plays a significant role in SSI variability under cumulus clouds.
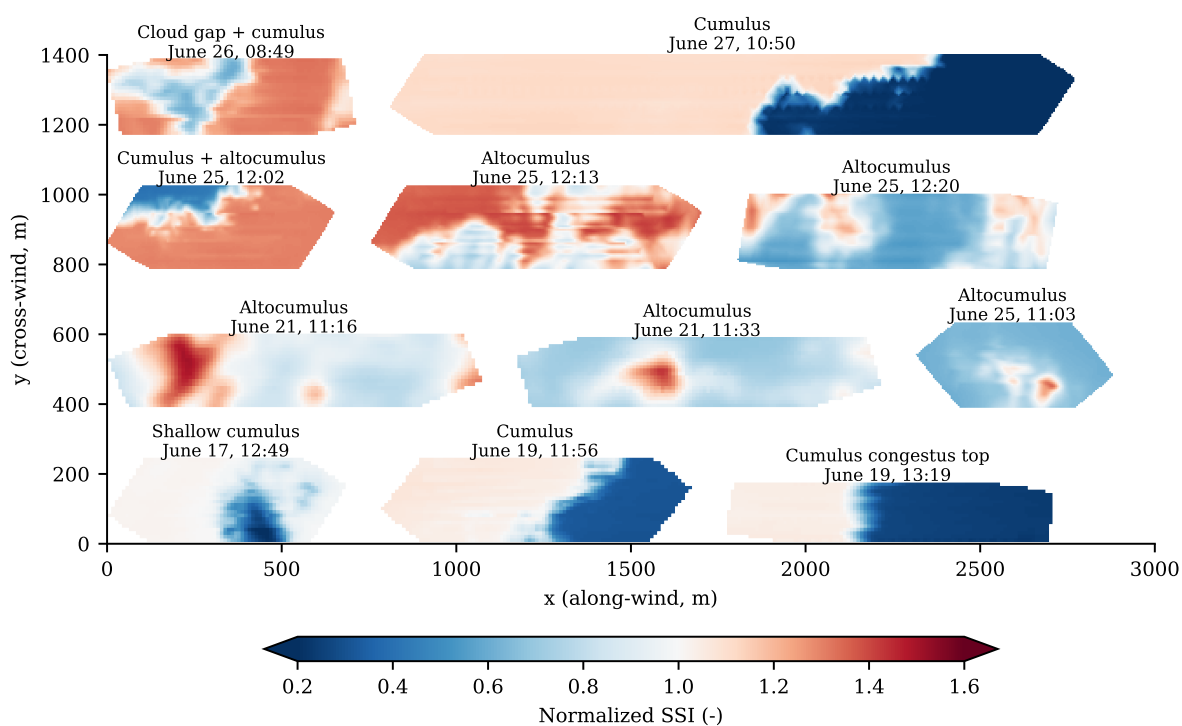
Figure 2. A collection of observed spatial patterns of surface solar irradiance. The patterns are spatially interpolated using temporal data as described in Mol et al. (2024) The labels indicate cloud type and date and time of occurrence (UTC), all in the year 2021. SSI is normalised with clear-sky SSI from McClear.

1.2 Proposed mechanisms

Cloud fields can manifest in a countless number of different configurations, each resulting in a unique surface irradiance field. It all cases, however, it starts with scattering of direct irradiance that is horizontally and diffusely redistributed onto the surface. We hypothesise that four key mechanisms by which solar radiation is horizontally redistributed can explain all the previously described prototype examples of SSI variability and irradiance enhancement peaks. These mechanisms are in part based on prior research and may be known under different names, hence we will review and (re)define the terminology. Figure 3 schematically shows the four mechanisms.

1.2.1 Forward escape

Between transparent and opaque clouds, there is a region of optical thickness where direct irradiance is scattered mostly only once or twice, if at all. In the case of cloud droplets, we are in the regime of Mie scattering. Thus, 90-99 % of scattering occurs within 5° of the forward direction (calculated using `miepython`, Prahl, 2023), depending on droplet radius and photon wavelength. Consequently, part of the direct irradiance is scattered to an area just besides the direct beam path, leading to irradiance enhancement if the direct path to this area is sufficiently cloud-free. Small isolated cumulus clouds, for example, were found by Robinson (1977) to affect an area of approximately 5 to 15° off the direct beam centre. This type of scattering occurs at cloud edges, where optical thickness approaches zero, and in other optically thin (parts of) clouds. Although scattering by individual cloud edges or transparent sections is limited, we expect this can become substantial for clouds or cloud fields with a significant amount of optically thin area. Altocumulus as shown in Figure 1b is an example of such an optically thin cloud field, indicated by the fact that direct irradiance is not fully attenuated.

1.2.2 Downward escape

Towards the upper limit of optical thickness, scattered radiation loses its forward component due to multiple scattering. While radiation then increasingly gets scattered back up, the large remaining part that does not get absorbed by the cloud is highly diffusely transmitted downward through the cloud, thereby create irradiance enhancements as it lands in adjacent cloud-free areas. We call this mechanism *downward escape*, a term introduced by Várnai and Davies (1999) (although their definition is expressed in terms of the horizontal photon transport bias in the 1D radiative transfer approximation).

Downward escape differs from *forward escape* in the location where the diffuse irradiance lands and how the diffuse irradiance coincides with direct to create extremes in SSI. Pecenak et al. (2016) show the transition between *forward escape* and *downward escape* clearly in 2D simulation experiments of rectangular clouds, with the peak of enhanced irradiance moving from near the projected shadow location to underneath the cloud as optical thickness increases. Optically thick but flat clouds, like the stratus and stratocumulus of Figure 1, are likely candidates for where this mechanism is a dominant factor in creation of SSI variability. Solar zenith angle will play an important role in the effectiveness of *downward escape* as a mechanism, as it determines to what extent direct irradiance can coincide with the peak in diffuse enhancement near or underneath the cloud.

1.2.3 Side escape

Optically thick clouds scatter a large part of the solar irradiance back to space. Similarly, under solar zenith angles higher than 0°, the sides of vertically structured clouds have the same effect, except due to the vertical orientation the scattering is

120   partially directed towards the surface. Segal and Davis (1992) described these effects of deep convective clouds as reflections, but Várnai and Davies (1999) refer to this phenomenon more accurately as backscattering. We will call it *side escape*, where cloud sides act as a region where photons diffusely escape after multiple scattering events, rather than reflecting radiation like a mirror.

We expect this mechanism to become effective as the total vertically oriented surface area increases compared to the hori-

125   zontal size of the cloud, typical in cases of deep moist convection. In such cases, optical thickness will generally be high and thus *forward escape* will be ineffective and most radiation escapes on the sunlit side. We thus also expect strongly asymmetric surface patterns of irradiance with vertically structured clouds due to diffuse irradiance being enhanced primarily on the sunlit side, as we find in the example in Figure 1c.

1.2.4 Albedo enhancement

130   Surface albedo can enhance the cloud-enhanced surface irradiance by multiple iterations of scattering between surface and cloud base. This mechanism may explain the extreme irradiance peaks observed during snow cover (high albedo) combined with broken cloud cover as reported by Gueymard (2017), or shown in Figure 1f. In a more general sense, this mechanism is known as *entrapment*, which can occur between any two scattering surfaces (Schäfer et al., 2016; Hogan et al., 2019). In this study, we focus on the entrapment of radiation between a surface (land or ocean) and a cloud (field). The effectiveness

135   of this mechanism, aside from higher surface albedo, will increase with cloud cover and optical thickness, required to scatter back reflected surface irradiance, up to the point where too little irradiance is available. Areas at the edge of stratus, gaps in stratocumulus, and perhaps large cumulus clouds are therefore candidates for significant *albedo enhancement*.

2   Simulation tools

We use a Monte Carlo ray tracer (MCRT) to simulate 3D radiative transfer within cloud fields overlying a surface. These cloud

140   fields either come from case studies run using large-eddy simulation (LES) where we simulate specific cloud types, or the cloud fields are manually created. The combination of the MCRT with these cloud fields allows us to isolate, to some extent, the contribution of the four mechanisms to the total surface irradiance variability. Information on creating the cloud fields and the ray tracer setup in general is given below. The details of each experiment are demonstrated in the next section. All model code, input data, and case setups are freely available, see our data availability statement at the end.
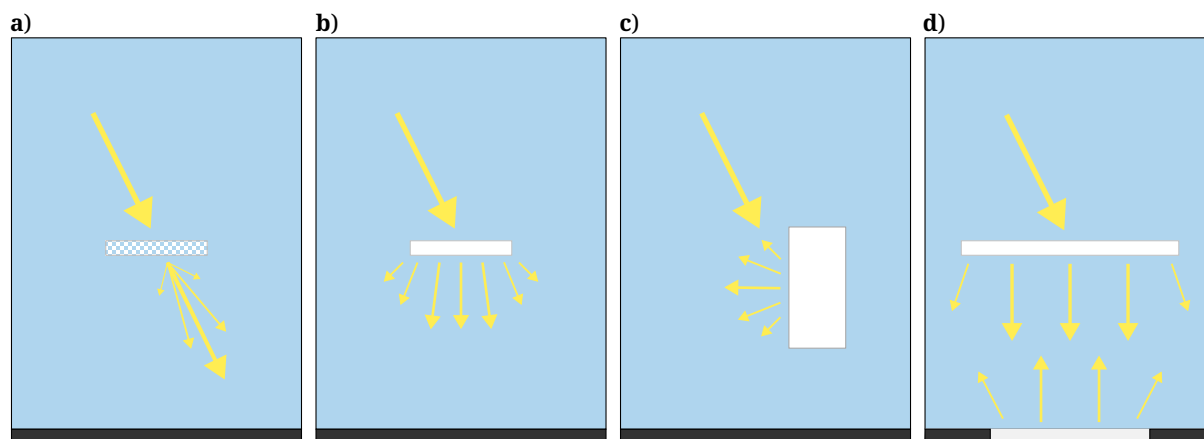
Figure 3. Schematic representation of the four proposed mechanisms that drive surface solar irradiance variability. From **(a)** to **(d)**, these are *forward escape*, *downward escape*, *side escape*, and *albedo enhancement*. Incident solar radiation is indicated by the large downward arrow, the other arrows indicate approximated average direction and intensity of scattered radiation. Surface albedo is indicated by the lightness of the surface. Only the arrows relevant to each mechanism are drawn.

2.1 3D radiative transfer

For simulating 3D radiative transfer, we use the GPU-accelerated version of the Monte Carlo ray tracer as introduced by Veerman et al. (2022). This model is based on the RTE+RRTMGP solver and is fast enough to run coupled to the LES, although in this study we use it in offline mode. One of the optimisations is a reduced spectral resolution, via smaller sets of so-called g-points, chosen in such a way as to have minimal impact on accuracy (Veerman et al., 2024). We use the 112 set for shortwave and the 128 set for longwave, halving the calculation time. This time is spent on spatial resolution, amount of rays, and the use look-up tables for an accurate Mie scattering phase function. The latter is important to resolve the narrow but dominant forward peak in scattering direction in the case of cloud particles.

For some cases, we solve radiative transfer online (i.e., coupled to the model) in order to simulate more realistic clouds that are radiation driven, such as altocumulus. We then use the standard RRTMGP solver with the independent-column approximation, which is much faster and good enough to create the cloud fields we want. Any analysis of irradiance we do only with the 3D MCRT.

We sample optical thickness τ from the MCRT, which gives a 3D field of τ per grid cell and wavelength band. τ is typically higher for longer wavelengths, but in this study we use the band centred in the visible spectrum, which contains the most energy. For a given amount of condensate, τ also varies with the effective droplet radius, which in turn depends on the droplet number concentration. We keep that number fixed at 2.5×10^8 m^{-3} for all cases, therefore an increase in τ with total liquid (or ice) mixing ratio is slightly offset by an increased effective radius. This will have no influence on the interpretation of our results.

2.2 Simulated and synthetic cloud fields

We use MicroHH in LES-mode as our cloud-resolving atmospheric model (van Heerwaarden et al., 2017). The model is
165   initialised with vertical profiles of temperature, moisture, and wind, either from observed soundings, reanalysis data, or from
idealised experiments based on literature. The lateral boundaries are periodic, and domain size and spatial resolution are case-
dependant. For the synthetic cloud fields, we start by initialising the model and then manually modify the cloud fields, either
by changing the temperature in a layer and letting the model condense water vapour, or by directly modifying the liquid (q_l) or
ice (q_i) fields.

170   We can manually move any cloud field up and down to test effects of cloud height, or test a range of optical thickness by
increasing or decreasing the amount of condensate while keeping the cloud geometry and location fixed. The surface is flat in
all simulations. Albedo is spatially homogeneous, wavelength-independent, and kept the same for direct and diffuse radiation.
In some simulations we prescribe homogeneous surface fluxes or run with online radiation and an interactive surface layer.

3   Experiments

175   What now follows is an overview of all cloud fields that we create. We run the 3D radiative transfer model on these cloud
fields and vary a set of parameters across a range of values, depending on the specifics of the experiment. These parameters
are surface albedo α, solar zenith angle θ, solar azimuth angle ϕ, cloud optical thickness τ, cloud altitude h, and cloud depth
d. For all configurations we run the radiative transfer model also once without clouds to estimate clear-sky irradiance (GHI$_{cs}$).
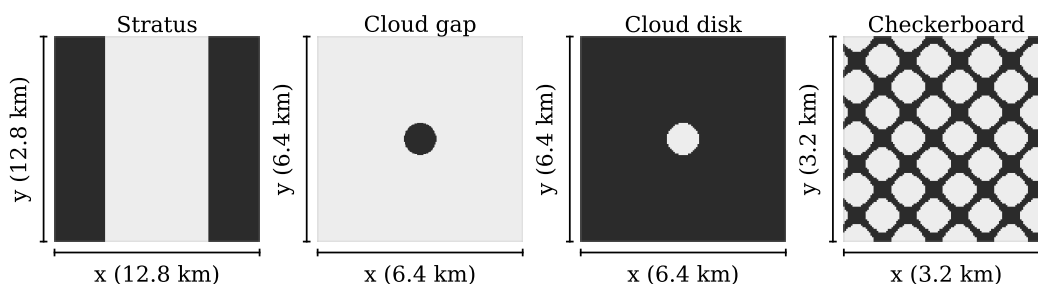
Figure 4. Top view of the synthetic cloud fields. Light greys indicate clouds, dark grays are the cloud-free areas. These clouds are thin
relative to their horizontal size (cloud depth varies between 25 m and 150 m). Cloud depth, altitude, and optical thickness depend on the case
and experiment. Note that the horizontal domains vary in size per case.

3.1   Synthetic cloud fields

3.1.1   Flat clouds

The horizontal geometry of four synthetic clouds fields are shown in Figure 4. The `stratus` case cloud is infinite in the
y-direction, is 3 grid-points thick (150 m), and sits at an altitude centred around 450 m above ground level (AGL). Vertically
integrated liquid water is 0.158 kg m^{-2} ($\tau \sim 19$). This is an idealisation of a case of stratus to clear-sky transition (and vice
versa), such as the example in Figure 1d.

For the `cloud gap`, we use the same configuration as in the `stratus` case, but now it stretches across the whole domain
and has a circular gap of 1 km in diameter in the centre. This resembles the cloud gap study by Yordanov (2015) and the
stratocumulus with a gap shown in Figure 1e.

The `cloud disk` case is the inverse of `cloud gap`, as can be seen in Figure 4, but only has a thickness of 1 grid-point
(50 m). That is unrealistically thin, but minimises the effect of *side escape*, as we manually vary its total condensate manually
to control optical thickness. Cloud disk altitude and diameter are also varied. This cloud is for testing the effect of a singular
patch of optically thin cloud, which may resemble a small cumulus, a transparent cloud edge, a single patch of altocumulus or
a piece of cirrus.

The `checkerboard` case features a checkerboard-like pattern of 100 m thick patches that are 500 m in diameter, with at
most a 150 m spacing in between patches, and sits centred around an altitude of 2850 m above ground level. This idealisation
is inspired by an observed case of altocumulus in FESSTVaL (see Section 3.2), with similar properties as shown in Figure 1b.

3.1.2   Vertical clouds

For studying the effect of cloud sides in the most simple way, we take the `cloud disk` and extend it vertically, effectively
creating a perfectly homogeneous and smooth cylinder. The cloud base is at 1000 m above ground level and cloud top varies
from 1500 to 12000 m. This case is an idealisation of a growing deep convective cloud (cumulus congestus) in an environment
free of wind shear, and therefore called `towering cumulus`. Figure 1c shows the passage of such a deeply developed
cloud, although there is also an anvil cloud present in this observation.

3.2   Simulated altocumulus

In this case, we simulate an altocumulus cloud field observed during the FESSTVaL campaign on June 21 (shown in Mol
et al. (2024) or partly in Figure 2). The model is initialised from a radiosonde at the observatory, which has a small layer of
nearly condensed air at approximately 2850 m and drier air above and below that layer. By increasing the relative humidity
beyond 100 % in this layer at the first time step, we force the creation of a thin layer of condensation. With small noise in
the vertical velocity field at initialisation, the model runs freely with coupled 1D radiative transfer, which develops the layer
of condensation into a thin field of dynamic altocumulus, as illustrated in Figure 5. Altocumulus requires a high simulation
resolution in order to resolve the altocumulus, as the vertical depth and horizontal cell structures are small. Domain size is
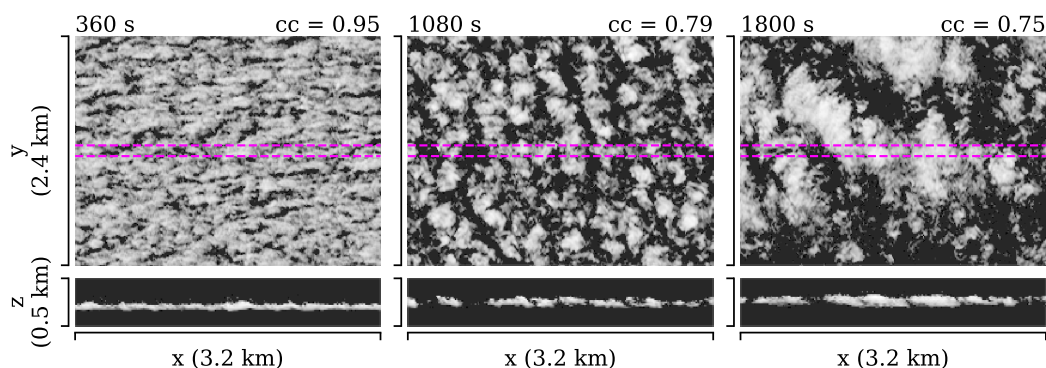
Figure 5. Simulated altocumulus evolution. The top row shows a top view of vertically integrated liquid water (q_l), the bottom row shows a side view of horizontally integrated q_l over a 200 m slice in the y-direction (marked by the dashed magenta lines). Cloud altitude is ~ 2800 m. The full domain is 6.4×6.4 km^2, only a subset is shown. Time step and cloud cover are labelled at the top.

210 therefore on the small side for an LES, with 6.4×6.4 km^2 (Δx, Δy = 12.5 m) and a vertical domain of 4.2 km (Δz = 16 m). After 1800 s, we get unrealistic wave growth in our periodic domain, which explains the large structures that emerge at this time step.

3.3 Simulated cumulonimbus

To extend `towering cumulus` to something more realistic, we run two versions of an isolated cumulonimbus. These are
215 adaptions of the idealised supercell simulation setup introduced by Weisman and Klemp (1982). In one simulation, we disable vertical wind shear, in the other we set it to 25 m s^{-1}, resulting in a straight vertical cloud and a tilted one, respectively. The horizontal domain is 153.6×153.6 km^2 (Δx, Δy = 200 m), with the domain top at 19.2 km (Δz = 150 m). A large domain is necessary to keep the cumulonimbus from scattering onto itself, due to periodic boundary conditions in the MCRT. Vertically and horizontally integrated liquid and ice water mixing ratios are shown in Figure 6 for three time steps during the growing
220 stage.

3.4 Simulated free convection

With the final simulation, called `free convection`, we aim to demonstrate what happens in a cloud field that is on the high-end of possible complexity, in contrast to the other experiments in this study. This simulation has a horizontal domain of 102.4×102.4 km^2 (Δx, Δy = 200 m), with the domain top at 19.2 km (Δz = 100 m). We initialise the simulation using
225 an observed conditionally unstable thermodynamic profile with low wind shear. We include online 1D radiative transfer to heat up an interactive land surface which will thermodynamically trigger convection. Figure 7 shows this evolution of `free convection` in three stages, from cumulus towards deep convection. After one hour, as the convective inhibition diminishes with daytime heating, widespread cumulus and cumulus congestus forms randomly, as there is no other forcing or form of
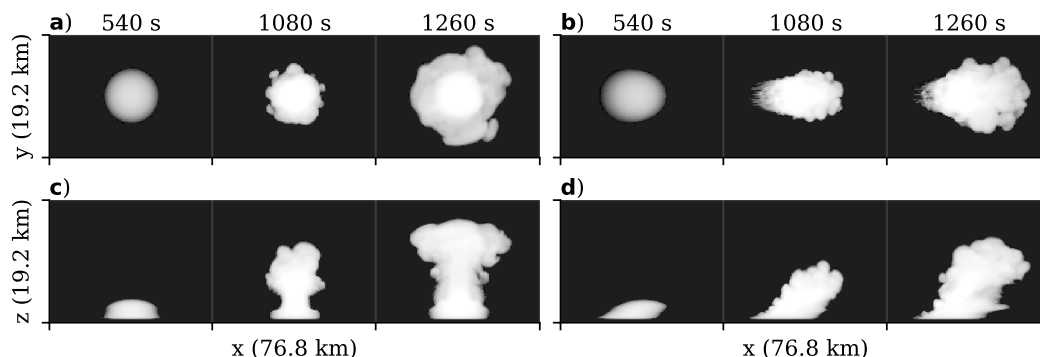
Figure 6. Two simulated deep convective updrafts. (**a, c**) show the updraft in shear-free conditions, (**b, d**) show the same updraft but with 25 m s^{-1} vertical wind shear. White colours indicate high values of liquid and ice water mixing ratios ($q_l + q_i$) integrated along the z or y-axis.

organisation. In subsequent hours, convection consolidates in a smaller number of strong deep convective clouds with large
230   anvils.
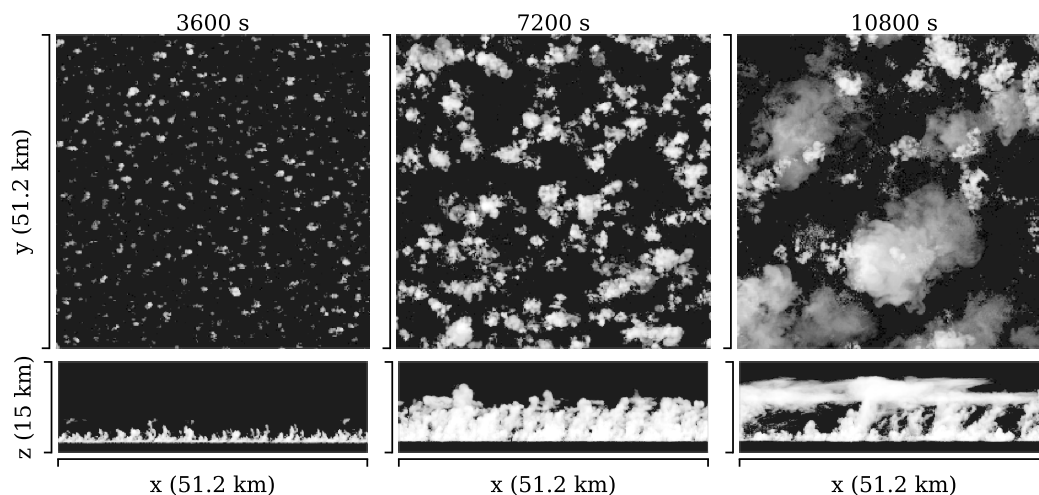
Figure 7. Simulated free convection. The top row shows the vertically integrated liquid and ice content ($q_l + q_i$), bottom row shows the same integral along the y-axis. Only a quarter of the full horizontal domain is shown.

4   Results

4.1   Cloud optical thickness controls which mechanism dominates

We will first demonstrate the relationship between the mechanisms of *forward escape*, *downward escape*, and *albedo enhancement*. The interplay between these three mechanisms using the `cloud disk` case is illustrated in Figure 8.

235   For low optical thickness ($\tau \approx 0.2$), radiation is primarily scattered into the projected cloud shadow at the surface. At high optical thickness ($\tau \approx 44.2$), the forward projection disappears, and instead a wide area centred underneath the cloud is diffusely enhanced. Albedo has no effect on the low end of the optical depth range, whereas it contributes significantly at the high end (~ 4 times more than *downward escape* at $\alpha = 0.8$). Intermediate values of τ show a transition from predominantly *forward escape* without *albedo enhancement* to *downward escape* with *albedo enhancement*.
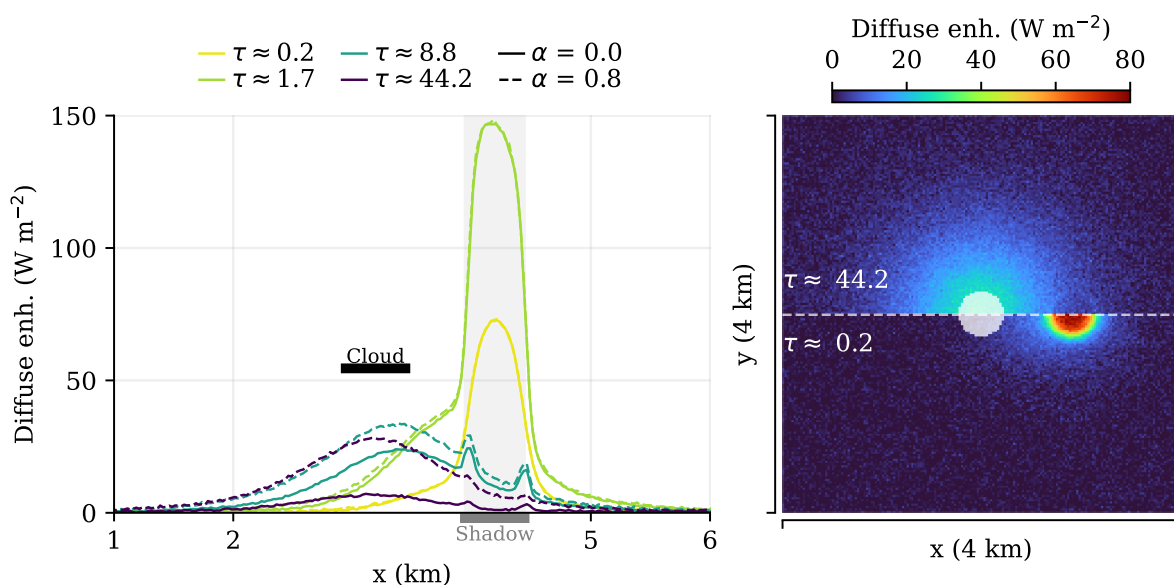
Figure 8. From *forward escape* to *downward escape*. A cloud disk at 1 km altitude with 25 meter depth and a 500 meter diameter scatters radiation coming in at a zenith angle of $45°$. Diffuse SSI enhancement is calculated relative to clear-sky values. The lines in the left plot are averaged over the middle 400 m in the y-direction, whereas the right plot shows the 2D surface field.

240   For this experiment, we can estimate a value for τ where the transition occurs as the point where the diffuse enhancement underneath the cloud exceeds that of within the projected shadow location. Estimated from Figure 8, this transition occurs between $\tau = 1.7$ and 8.8. Numerically, by simulating the values of τ in this transition range, we find *downward escape* takes over at $\tau > 6.3$, or $\tau > 5.4$ when *albedo enhancement* is included ($\alpha = 0.8$). We keep these numbers for τ in mind for the next sections as an estimate for the scattering regime we are in terms of mechanism.

245   What this experiment illustrates is that when *forward escape* dominates in a cloud field, *albedo enhancement* is negligible. Furthermore, for a uniform cloud, *downward escape* and *forward escape* only co-occur in the intermediate range of optical thickness. In more complex clouds or cloud fields, in which low and high optical thickness are common and close together, these mechanisms may still co-occur.

4.2   How the mechanisms work in stratus, cloud gap, and checkerboard

250   We will now further describe the *albedo enhancement* and *forward escape* mechanisms using the synthetic cloud fields. In Figure 9a-c, we show the resulting SSI pattern for the `stratus`, `cloud gap`, and `checkerboard` cases. All three resemble the patterns of diffuse, direct, and total SSI from the observations in Figure 1b,d, and e, respectively.

Given the optical thickness regimes we estimated in the previous section, the patterns for `stratus` and `cloud gap` are driven exclusively by *downward escape* in the absence of albedo. Diffuse irradiance is primarily enhanced underneath the

255   cloud, with the largest enhancement found just at the transition where direct irradiance appears. Increasing the zenith angle in the `stratus` case further shifts the direct irradiance underneath the cloud on the sunlit side where diffuse irradiance is enhanced the most, which maximises the possible irradiance enhancement in this configuration.

For a 100 m diameter cloud gap, diffuse irradiance is uniformly enhanced below the cloud field, and any direct irradiance would coincide with the peak enhanced diffuse (Figure 5). Widening the gap would reduce the diffuse enhancement underneath

260   that gap, as we are in the *downward escape* regime, and thereby make the irradiance enhancement more dependent on having a high enough solar zenith angle to optimally position the direct irradiance with respect to peak diffuse enhancement. For a gap diameter that is close to the cloud vertical depth, direct irradiance will be unable to pass through and create any irradiance enhancement at higher solar zenith angles, as is the case for $\theta = 60°$ in Figure 9h.

The `checkerboard` case is different, as the cloud field is optically thin, which results in a pattern that is dominated by

265   *forward escape*, ignoring potential *albedo enhancement* for now. Diffuse irradiance is enhanced almost uniformly underneath the cloud field despite dominant *forward escape*. This is due to the high altitude of the cloud (2850 m), which allows the forward diffuse peaks of individual cloud patches to be spread over a larger surface area and merge together. As a result, irradiance enhancement is approximately 45 % in the sunlit gaps between the cloud patches with only slight variations. We will now further investigate the *albedo enhancement* and *forward escape* mechanisms in these cloud fields.

270   ## 4.3   Albedo significantly enhances SSI under optically thick clouds

We quantify the *albedo enhancement* (AE) in the presence of a cloud for a specific surface albedo (α) as $AE_\alpha = IE_\alpha - IE_{\alpha_0}$. Here, IE_α is the cloud-enhanced surface irradiance for a given albedo α, i.e., $SSI_\alpha - SSI_{\alpha,cs}$. α_0 is the reference albedo of 0, representing the cloud-enhanced irradiance without any *albedo enhancement*. AE_α is shown in Figure 9 for the `stratus`, `cloud gap`, and `checkerboard` cases.

275   The simplest effect can be seen in the patterns in Figure 9a-c, where the dotted lines are $\alpha = 0.8$, which all show a significant increase in diffuse irradiance and minor reduction in direct irradiance (normalised by their respective clear-sky values). The high cloud cover and optical thickness of the stratus cloud in the `stratus` and `cloud gap` cases result in significant *albedo*
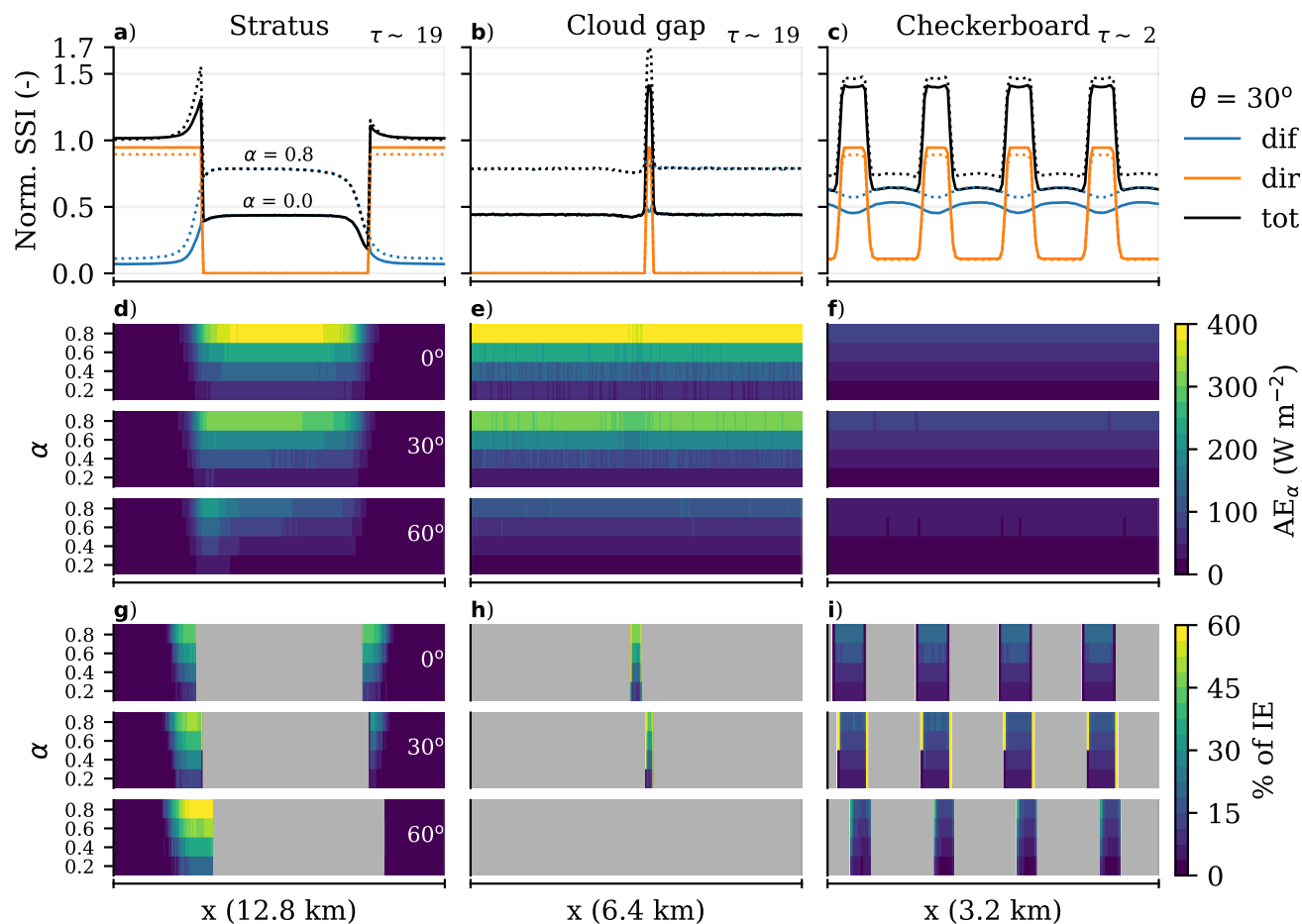
Figure 9. Surface patterns for the stratus, cloud gap, and checkerboard cloud fields. The top row shows the diffuse, direct, and total surface solar irradiance along the x-axis and averaged over (a part of) the y-axis. The middle row shows *albedo enhancement* for a given albedo (AE_α) as the irradiance enhancement relative to $\alpha = 0$ for $\alpha \in [0.2, 0.8]$. The bottom row shows the relative contribution of AE_α to the total enhancement of irradiance IE_α. Solar zenith angle is $30°$ for the top row, or 0, 30, and $60°$ for the other subplots.

enhancement. Firstly, albedo enhances the diffuse irradiance most where local cloud cover is highest, which explains the patterns in Figure 9d and e. Once again, this shows that low cloud optical thickness renders *albedo enhancement* negligible, as
280   shown by the weak diffuse enhancement in the `checkerboard` case (even for $\alpha = 0.8$).

Figures 9g-i show the relative contribution of *albedo enhancement* to the total IE, with shaded areas greyed out. This shows that at a modest albedo of 0.2, the albedo accounts for 10 % of the total IE in the stratus and cloud gap cases. For high albedo, this can increase to as much as 60 % ($\alpha = 0.8$) for the `stratus` case at $\theta = 60°$. Under such conditions, direct irradiance lands further underneath the stratus cloud on the sunlit side, and thereby adds a significant amount of radiation that gets trapped
285   between the cloud and the surface.

In the `cloud gap` case, *albedo enhancement* is similar to stratus. While the cloud gap case would have a higher potential for *albedo enhancement*, given that direct irradiance nearly always lands underneath the peak diffuse enhancement, the gap limits the amount of direct irradiance available for multiple scattering. Still, while the relative contribution of *albedo enhancement* to IE is approximately 10 to 45 %, the total IE is larger in this case, reaching 70 % for $\alpha = 0.8$ at $\theta = 30°$.

For optically thick clouds and high cloud cover, *albedo enhancement* can thus be significant, already contributing $\sim 10\%$ to the total IE at a modest albedo of 0.2. The `checkerboard` case shows only a 10 to 15 % contribution of *albedo enhancement* to IE for the most extreme case of $\alpha = 0.8$. This is consistent with the low optical thickness of the cloud field and thus limited entrapment. At lower albedo, the contribution of *albedo enhancement* is negligible, meaning the extremes in SSI in this case are nearly exclusively driven by *forward escape*.

4.4 Forward escape enhances SSI for low clouds or high cloud area

As previously discussed in Section 4.1, *forward escape* results in scattered irradiance that closely follows the direct beam, of which a fraction lands next to the partially shaded area, creating irradiance enhancement. Hence, peak irradiance enhancement is low, as most scattered radiation falls within the projected shadow of the cloud (see Figure 8). We think this is why SSI is barely, or not at all, enhanced near the edges of cumulus clouds, as can be seen in the spatial patterns in Figure 2. The areas of low optical thickness in cumulus clouds, found at the edges or for the whole of the smallest shallow cumuli, are so small compared to the whole hemisphere from which radiation originates, that *forward escape* contributes little to irradiance enhancement or SSI variability. So how can *forward escape* still be effective in creating (extreme) SSI variability?

4.4.1 How forward escape effectiveness varies with cloud altitude and area

To further understand *forward escape*, we will study its relationship with cloud altitude and area. For this, we create `cloud disks` of 100 and 1000 m in diameter with an optical thickness of $\tau \approx 2$. Figure 10 illustrates the effect of both cloud altitude and area. First, for the 1000 m diameter `cloud disk`, the peak diffuse enhancement or total irradiance enhancement is increased by at least a factor of 2 compared to the 100 m diameter one. Second, by lowering the altitude of the cloud disk, the forward scattered irradiance is spread out over a smaller area and thus peak enhancement in both diffuse and total irradiance increases. The total irradiance enhancement is always lower than diffuse enhancement, because for low optical thickness most scattered irradiance still falls within the projected shadow of the cloud.

A small area of optically thin cloud at low altitude is still not very effective, as the peak in irradiance enhancement is only able to exceed 5 % with respect to clear-sky at an altitude below 500 m. Conversely, the larger cloud disk already exceeds clear-sky SSI by 10 % at 6 km, and peaks at 25 % around 500 m altitude. The small decrease below 500 m is likely due to the cloud disk being so close to the surface that scattered radiation can not spread out horizontally enough to maximally combine diffuse and direct irradiance. To create more extreme SSI values, we can further increase the cloud area and place it at a higher altitude to maximise the combination of all scattered irradiance. Essentially, this is what we think happens in altocumulus, which we will now demonstrate.
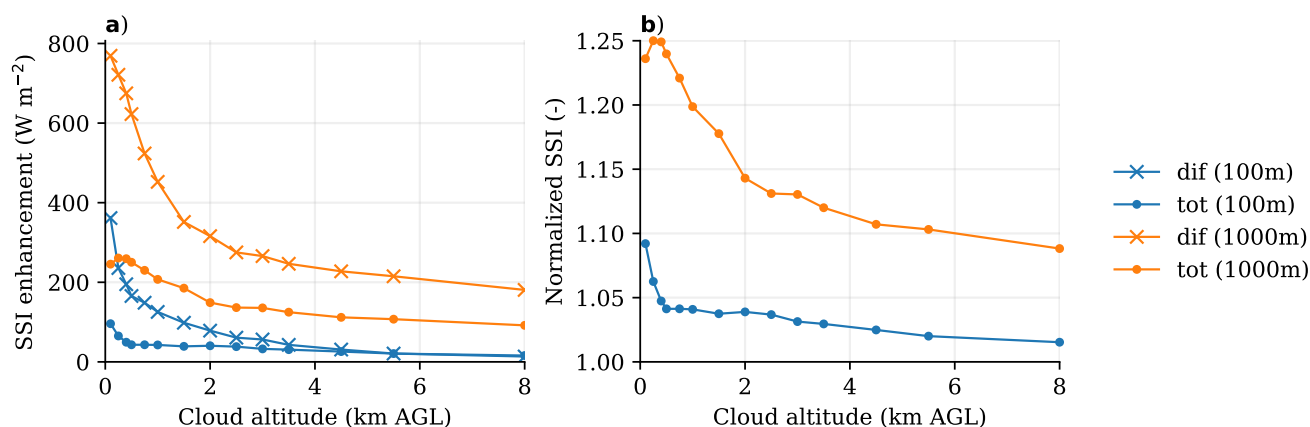
Figure 10. Effects of *forward escape* with varying cloud altitude and cloud diameter. Domain maxima for cloud diameters 100 m and 1000 m are shown here. In **(a)** the absolute surface solar irradiance (SSI) enhancement with respect to clear-sky (total or diffuse), and in **(b)** the total SSI enhancement normalised by clear-sky values. Solar zenith angle is $0°$, surface albedo is 0, and cloud optical thickness $\tau \approx 2$.

4.4.2 Why altocumulus fields create extreme SSI peaks

The simulated altocumulus fields affect the surface solar irradiance fields very similar to that of the `checkerboard` cloud field. Figure 11 illustrates the general patterns and dependence on solar zenith angle. Diffuse irradiance is relatively constant throughout the domain, with strong irradiance enhancements in the gaps between cloud patches. Higher total cloud cover (0.71 to 0.94), all of which has low optical depth ($\tau \sim 0.4$ to 0.6 on average), increases the total enhancement of diffuse and thereby increases the magnitude of the irradiance peaks. Higher cloud cover reduces the probability of these peaks occurring, however. Solar zenith angle affects the results primarily through reducing the effective size of the cloud-free areas, while increasing the relative magnitude of the enhancement.

The effect of albedo is also very small in for the simulated altocumulus, despite high cloud cover. At an albedo of 0.8, the contribution to the irradiance peaks is only $\sim 15\,\%$ (varying slightly with cloud cover and zenith angle). This means that the altocumulus field we simulate is nearly exclusively generating extreme irradiance variability by *forward escape*, even in high-albedo conditions. The 3D radiative effects should therefore be relatively simple to reproduce by a diffuse forward projection of the clouds combined with attenuated direct irradiance, and may not require an expensive model like we are using.
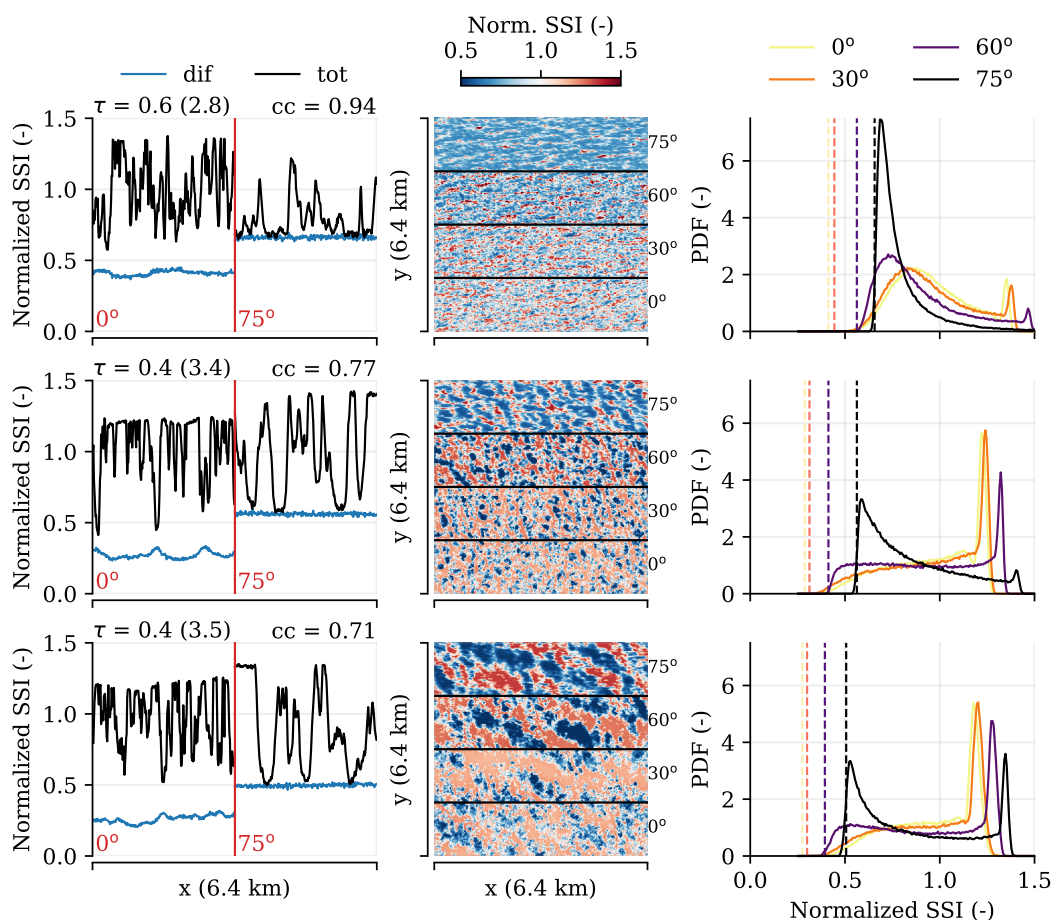
Figure 11. Surface irradiance effects of simulated altocumulus. The first column shows a section through the centre of the domain along the x-axis for a solar zenith angle of 0° and 75°. The centre column shows for all simulated zenith angles the total surface irradiance field. The right column shows the probability density functions of these fields, and adds the locations of the diffuse peak probability with the dashed lines. The rows are individual time steps (360, 1080, and 1800 s), accompanied by decreasing cloud cover (see also Figure 5). Surface albedo is 0.

4.5 How cloud depth enhances SSI

We will now introduce the fourth mechanism, *side escape*, by analysing vertically developed clouds, starting with the synthetic towering cumulus and followed by two types of simulated and isolated cumulonimbus. For all experimental results that follow, the Sun is located in the west (azimuth angle of 270 degrees), with a variable zenith angle θ, and albedo set to 0. Furthermore,

335   integrated optical thickness is, for the most part, well beyond the *forward escape* regime in all experiments (typically $\tau > 50$), even when considering horizontally integrated optical thickness. There are two exceptions where *forward escape* still occurs. The first is at non-zero zenith angles, where direct irradiance passes through the corners of an (optically thick) cloud. The second is for the edges of the simulated cumulonimbus, which are in or near the *forward escape* regime ($\tau < 10$), even when vertically integrating τ. Before we further discuss these effects, we describe the general patterns of SSI for the simpler case of

340   `towering cumulus` and the role of cloud depth in these patterns.
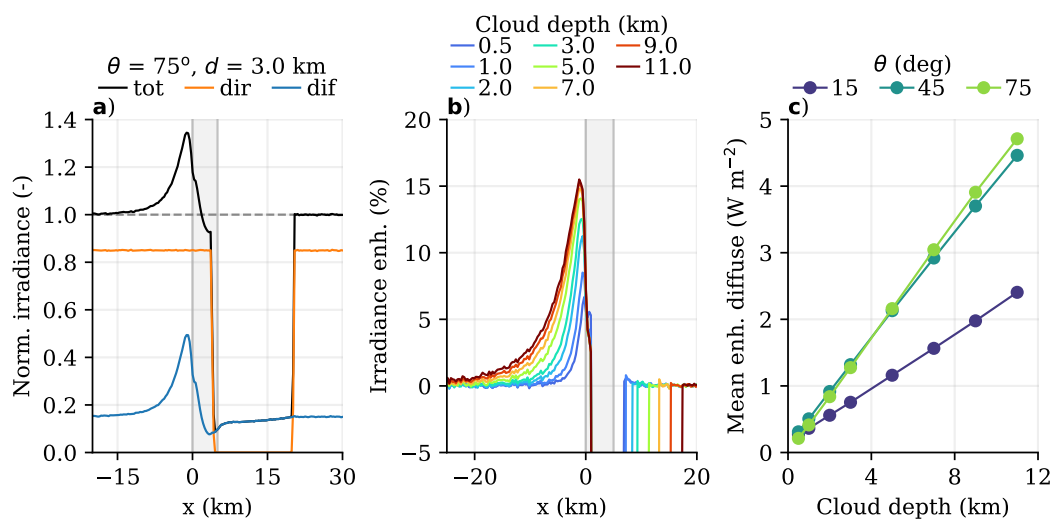
Figure 12. SSI pattern for an idealised towering cumulus. An example surface irradiance pattern is shown in **(a)**. The effect of increasing cloud depth on this pattern is shown in **(b)** for a solar zenith angle of $45°$. Mean diffuse enhancement on the sunlit side of the cloud is shown in **(c)** for varying cloud depths and zenith angles. Cloud base is at 1000 m, surface albedo is 0. The x-axis is relative to the location of the sunlit cloud side.

4.5.1 Synthetic towering cumulus

A key feature of the SSI pattern in the presence of a vertically structured cloud is the significant irradiance enhancement on the sunlit side and (near) absence of enhancement on the shaded side. Figure 12a illustrates this for a `towering cumulus` 3 km in depth, 5 km diameter, and a $75°$ solar zenith angle. The SSI pattern is similar to the observed time series of a cumulonimbus

345   passage in Figure 1c, with a peak of enhanced diffuse irradiance on the sunlit side, a reduction underneath the cloud, and a

return to (almost) clear-sky levels of SSI afterwards. As the `towering cumulus` increases in vertical depth, the rate of increase of the peak enhancement diminishes progressively, converging to a maximum of 15 % (for $\theta = 45°$, Figure 12b).

However, while the peak enhancement levels off, the area of influence extends further out, with IE still being a quarter of peak levels 10 km west of the sunlit side for the 11 km deep cloud. The total amount of diffuse enhancement in the domain scales linearly with cloud depth ($r^2 \approx 0.99$, Figure 12c). Both the levelling off of the peak irradiance enhancement and increased horizontal extent of the surface pattern is explained by additional scattering occurring at increasingly higher altitude, which result in additional scattered diffuse radiation being spread out over a larger horizontal area on the surface.

Total scattered irradiance on the half of the domain that is on the sunlit side of the cloud, including increased top of domain outgoing radiation, is close to 100 % of the scattered direct irradiance intercepted by the cloud side. Scattering off of cloud sides appears to be symmetrical in the vertical, at least for a perfectly straight and smooth cloud side, as half the radiation lands on the surface and half is radiated upwards out of the domain.
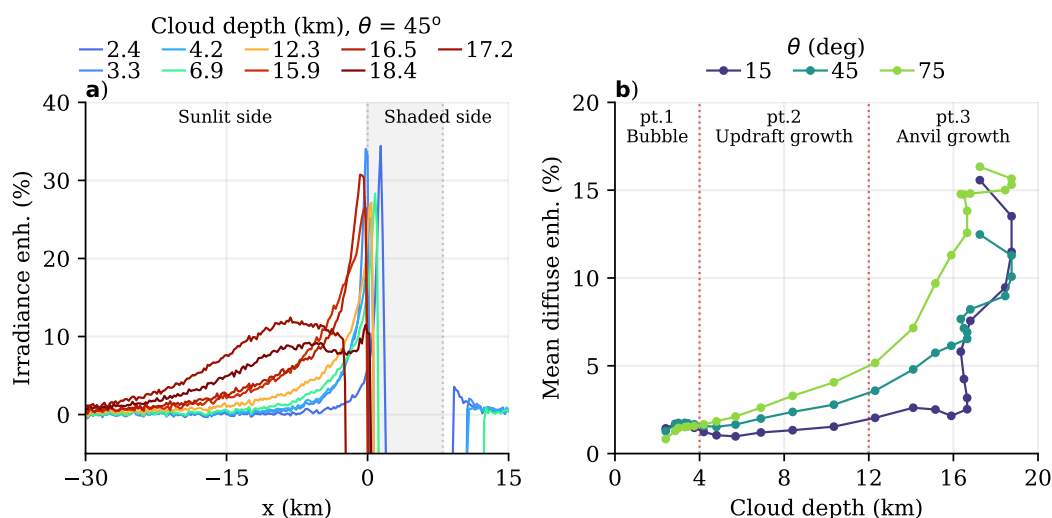
Figure 13. SSI patterns for a cumulonimbus in a shear-free environment. The pattern in **(a)** is an average over the updraft width in the y-direction. The grey shading marks the approximate position and width of the updraft. Domain-mean surface diffuse enhancement on sunlit half is shown in **(b)** as function of cloud depth. Simulation evolution is marked by three phases (further explained in the text). Surface albedo is 0.

4.5.2 Simulated cumulonimbus

In the cumulonimbus simulations, the updraft cloud is more turbulent and textured than the perfectly smooth `towering cumulus`. The SSI patterns remain largely the same, with significant enhancement only on the sunlit side close to the cloud and increased enhancement over a large area with increased cloud depth (Figure 13a). However, the peak irradiance enhancement in the shear-free case is ~ 30 % and remains fairly constant with increased cloud depth, unlike the `towering cumulus`. Once

the anvil cloud reaches far enough out to completely shade the updraft from direct irradiance, peak irradiance enhancement reduces from 30 to 10 %, visible in the last two simulation snapshots in Figure 13a (18.4 and 17.2 km).

The dynamic evolution of the simulated cumulonimbus also alters the relationship of total diffuse enhancement we observe in the domain. We identify with three distinct parts, illustrated in Figure 13b. Initially, in part 1, the warm bubble that triggers the convection is wider than it is tall, and therefore diffuse enhancement is driven by *forward escape* and *downward escape*. During updraft growth, in part 2, the relationship between cloud depth and diffuse enhancement returns to the linear relationship observed for the `towering cumulus`. For higher zenith angles, diffuse irradiance is enhanced relatively more with cloud depth than for conditions with near overhead Sun ($\theta = 15°$). Finally, in part 3, the anvil growth takes over and accelerates the domain mean diffuse enhancement, whereas peak irradiance enhancement decreases as the updraft itself becomes shaded.

The disappearance of the peak irradiance enhancement due to anvil shading hints to *downward escape* and *forward escape* being the mechanisms driving the irradiance extremes, not *side escape*. In support of this, Figure 14 illustrates the relative position of the diffuse and total enhancement with respect to the cloud and direct irradiance path, with and without anvil shading. Without anvil shading, the peak diffuse enhancement lies directly underneath, and not in front of, the cloud edge at the sunlit side. Here, only *forward escape* and *downward escape* can occur, and thus these mechanisms drive peak enhancement. Most diffuse enhancement in front of the cloud comes from *side escape* before the anvil forms, as this scales with cloud depth. Once the anvil spreads out, it takes over the *side escape* mechanism and further enhances diffuse SSI by *forward escape* and *downward escape*, stretching out for > 20 km relative to the cloud centre.
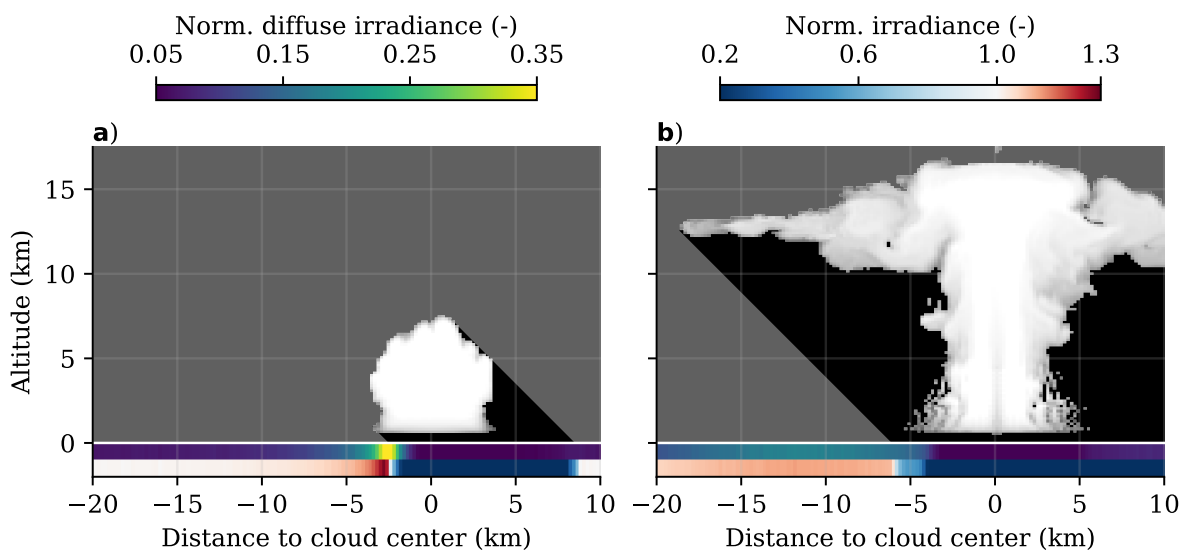
Figure 14. SSI peak location and the effect of anvil shading. An example surface irradiance pattern from the shear-free cumulonimbus simulation is shown at two time steps, one with and one without anvil shading. Solar zenith angle is $45°$, surface albedo is 0. The cloud is visualised by a liquid and ice-water cross-section, taken exactly halfway through the cloud in the y-direction. Dark grey shading illustrates the area where direct irradiance is 0. Normalised with clear-sky surface solar irradiance.

Tilting the updraft (with vertical wind shear) does not qualitatively change the SSI pattern with respect to the shear-free
380   simulation, as illustrated in Figure 15. However, the relationship of domain averaged diffuse enhancement with cloud depth is
not linear anymore during the updraft growth. Likely, the tilt results in a non-linear relationship between total sunlit cloud area
as function of cloud depth, unlike the shear-free and idealised versions of this experiment.

Solar azimuth angle becomes important in this simulation, since the simulated cumulonimbus is not rotationally symmetric
anymore, especially once the anvil develops and gets advected downwind, away from the updraft base. With the Sun in the
385   west (upwind), there is no interference from the anvil cloud, and thus the peak irradiance enhancement underneath the cloud
edge on the sunlit side remains. Illumination on the eastern (downwind) side of the cloud is quickly obscured by anvil shading.
With the Sun in the south, the updraft base stays sunlit with a slight extension of the anvil, and so peak and total irradiance
enhancement on the sunlit side is among the highest. There is no clear relationship between solar azimuth angle and total
diffuse enhancement, however. We think any differences will relate to the specific shape of the cloud and its orientation with
390   respect to the solar angle, and hence will not generalise beyond this case.
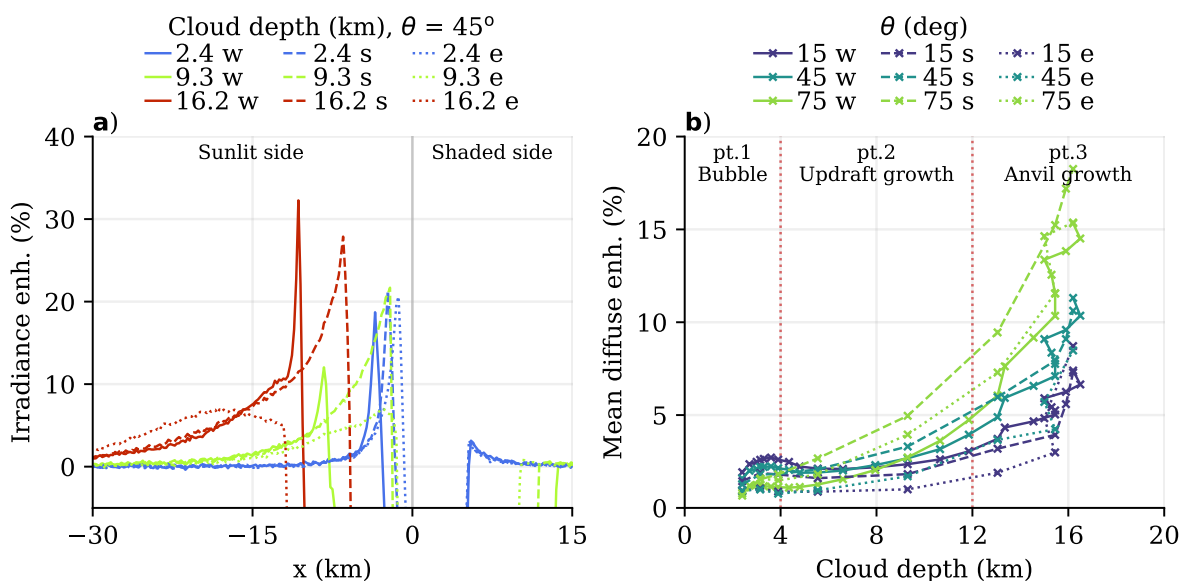
Figure 15. The effect of wind shear and solar azimuth angle on SSI in a simulated cumulonimbus. The surface diffuse enhancement is
shown in **(a)**, similar to Figure 13. Now, the x-coordinate is centred in the middle of the domain rather than the cloud centre or side, so the
pattern shifts as the cloud moves or dynamically evolves, and as the solar azimuth angle changes. The sun shines from the west, south, or
east, labelled with w, s, and e, respectively. Data is rotated such that the x-coordinate follows the solar azimuth angle.

4.6 Free convection integrates all mechanisms

All clouds presented so far are either flat and horizontally structured, or vertically structured but isolated. In the last experiment, we want to give a first look at what happens under highly complex cloud fields, for which we use the simulated `free convection` case. After three hours of simulation time, the cloud field features a handful of deep convective clouds with
395 large anvils, about as many newly developing cumulus congestus, and numerous cloud remnants of previous convection distributed throughout the domain. This cloud field and resulting SSI field for an intermediate solar zenith angle of 45° is shown in Figure 16.

One similarity with the cases of isolated deep convection is that peak irradiance enhancement occurs on the sunlit side of deep convective clouds, but in this case only when there is no shading from other nearby clouds. In regions furthest away from
400 clouds, the enhancement decreases to a local minimum of $\sim 10\%$ (e.g., x = 25 km, y = 80 km). Regions with the highest irradiance enhancement are enclosed by an optically thick updraft to the east and a high degree of cloudiness in the other directions (e.g., x = 20 km, y = 20 km). *Forward escape* plays a partial role in this, but it can originate from multiple clouds and cloud layers. To mark these parts of the cloud field, we show areas where $\tau < 6$ at an altitude above 7 km in blue, and in red when below 7 km in Figure 16b. These cover 20% and 10% of the domain, respectively, and can overlap. Other cloud
405 areas have high enough optical thickness for *albedo enhancement* to contribute.

What this simulation shows is that all four mechanisms can be active at once and be further complicated by having multiple deep convective clouds. The latter can be destructive to peak irradiance enhancement by anvil shading, or shading of other clouds, but also constructive by providing additional diffuse irradiance from multiple cloud edges towards areas already strongly enhanced by a sunlit cloud base. Finding an analogue in observations is unfortunately difficult, with the cloud field
410 being this complex and the SSI patterns this large.

5 Conclusions

In this study, we performed numerical experiments to understand which main mechanisms drive surface solar irradiance extremes across a diverse set of prototype cases based on observations. We formulated four mechanisms, based on observations and prior research, that can explain the observed irradiance extremes: *forward escape*, *downward escape*, *side escape*, and
415 *albedo enhancement*. First, we will synthesise the results of all the experiments. Then, we will discuss some limitations and potential future research directions, with a first look at what happens in the complex, multi-layered cloud field of unorganised deep convection.

5.1 Synthesis of results

For clouds or cloud fields that are much wider than tall, such as stratus or altocumulus, we find that the mechanisms driving
420 SSI variability depend on cloud optical thickness τ. The transition zone between *forward escape* and *downward escape* is estimated to be between $\tau = 5.4$ and 6.3, for high and low surface albedo, respectively. In the presence of optically thin clouds
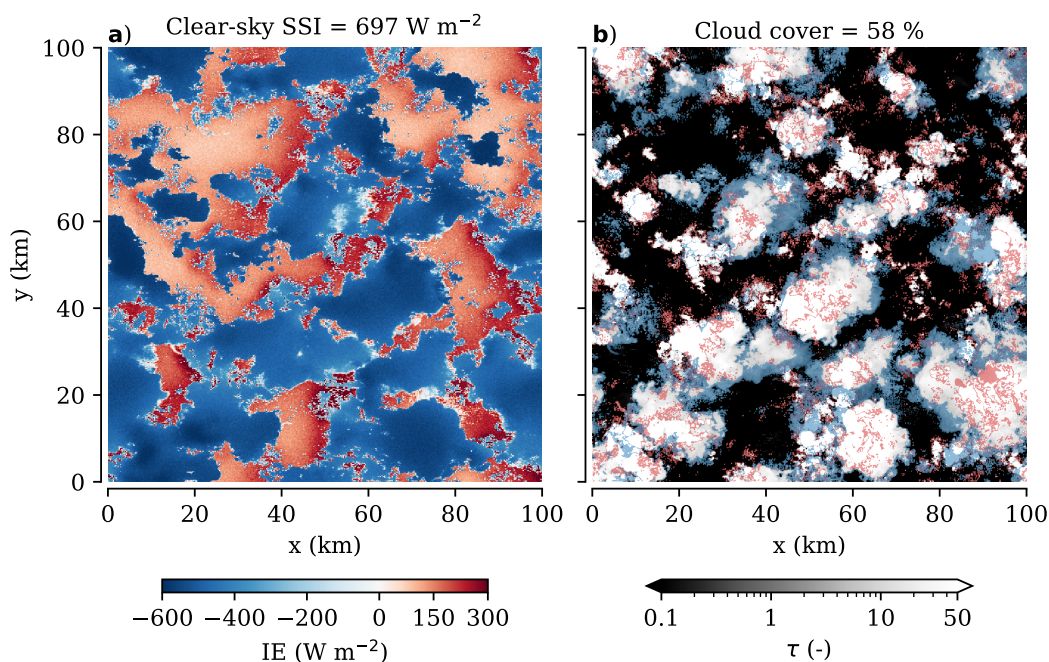
Figure 16. Irradiance enhancement in free, deep convection. Total surface solar irradiance relative to clear-sky is shown in **(a)**, for a solar zenith angle of $45°$. Vertically integrated cloud optical thickness τ is shown in **(b)**. Clouds with $\tau < 6$ at an altitude above 7 km are marked in blue, or in red when below 7 km, to indicate regions where *forward escape* occurs.

($\tau < 6$), *forward escape* drives enhancement of diffuse irradiance, which largely follows the path of direct irradiance. Cloud altitude determines the extent of horizontal smoothing of the forward scattered irradiance. It leads to smaller areas of higher extremes at lower altitude compared to more uniform diffuse irradiance from scattering at higher altitude. Increasing the cloud
425 area increases the total amount of scattering, which explains the extremes observed and simulated in cloud fields with gaps like altocumulus.

For optically thick clouds ($\tau > 6$), irradiance is scattered uniformly downward, leading to irradiance extremes near cloud edges or cloud gaps. In the transition zone ($\tau \sim 6$), both *forward escape* and *downward escape* contribute to the irradiance extremes.

430 Once *downward escape* starts to play a role in SSI variability, the clouds are optically thick enough to produce multiple scattering events between the surface and cloud. Under high albedo conditions and optically thick cloud cover, diffuse irradiance is then further enhanced by surface albedo, and accounts for 10 to 60 % of the total irradiance enhancement depending on low (0.2) or high (0.8) albedo conditions, respectively. The `checkerboard` case shows little contribution of *downward escape*, thus *albedo enhancement* is negligible and only contribute to a further 10 % increase in diffuse irradiance for the highest surface
435 albedo conditions (0.8).

For isolated deep convective clouds, the sides of the cloud act as a region where photons diffusely escape, leading to large areas (~ 20 km) of relatively weak irradiance enhancements ($\sim 5\%$) on the sunlit side of the cloud. Underneath the cloud edge, at non-zero solar zenith angles, the peak enhancement is 10 to 30 %, and is driven by *downward escape* and *forward escape* rather than *side escape*. Anvil shading onto the updraft of the cloud removes the local irradiance extreme found near the sunlit cloud edge.

5.2 Outlook

We have purposefully focused the majority of this study on understanding prototype cases of SSI variability that occur in single-layer horizontal or isolated vertical cloud fields. One reason for this is that observing the 3D structure of more complex cloud fields is very difficult, as ground-based observation typically can not see beyond the bottom of the first layer, and satellite observations not beyond the top of the highest layer. Reconstructing a prototype case to then numerically simulate brings too much uncertainty with it to disentangle the extra complexity that such a 3D cloud field provides. This is another way of saying that we do not have the observations to validate the case of simulated `free convection`, contrary to all other simulations in this study.

However, a next step would indeed be to expand this research to multi-layered cloud fields and non-isolated deep convective clouds. Multi-layer cloud fraction is estimated to be between 10 and 50 % globally (Li et al., 2015), highest around the equator and mid-latitudes, and mostly because of high clouds. It would be interesting to find out whether multi-layered cloud fields are additive in their effect on SSI, or if entrapment between layers results in significant non-linearity. As for non-isolated deep convection, a first analysis we did into this direction suggests such cloud fields produces irradiance extremes from a combination of all mechanisms formulated in this study. Furthermore, there is the additional effect of multiple clouds constructively or destructively combining their effects on SSI.

To better quantify how much each mechanism contributes to the total SSI variability, it would help to keep statistics of scattering events and direction of travel of photons. This is possible with ray tracing, but simply is not implemented in our model. Instead, we estimated the transition between *forward escape* and *downward escape* by sampling the diffuse SSI field given a cloud. With the extra statistics, however, this transition between mechanisms can be more precisely defined.

We have not separated out the effects of liquid and ice phase condensate in our analyses, but the contribution of each scattering mechanism may depend on cloud droplet phase as well. For example, this may be relevant for the cloud tops and anvils of cumulonimbus clouds in the upper troposphere, or in mixed-phase clouds, as is often the case in altocumulus (Barrett et al., 2017). The simulations with deep convection do not suggest there is a significant change in how the mechanisms behave once ice appears, however. Primarily, it is the overall 3D cloud geometry and optical thickness that determine how the SSI is affected.

In summary, the findings of our experiments provide a foundation to understand which mechanisms are at play for any given cloud or cloud field that is either flat and horizontally structured or isolated and vertically structured. We believe this is a good starting point for future analyses of surface solar irradiance under cloudy conditions, whether those are simple but more observationally constrained conditions than our prototypes, or perhaps maximum complexity like unorganized deep convection.

470 In any case, the diversity of SSI patterns and extremes with the set of cloud fields we have demonstrated should motivate others
to consider cloud fields beyond a single type, and likely include effects of surface albedo.

Code and data availability. BSRN time series data is described in Mol et al. (2023b), and is available in Knap and Mol (2022) and Mol
et al. (2022). Spatial SSI data of FESSTVaL is described in Mol et al. (2024), and is available in Mol et al. (2023a). Model code, setup
files, output data, Veenkampen time series data, spatial SSI patterns, and python scripts to analyse and visualise the data are available at
475 https://doi.org/10.5281/zenodo.11503609.

Author contributions. WM designed the methodology, performed the analyses, wrote the manuscript, and curated the data. CvH concep-
tualised the overarching research aim, acquired the funding, reviewed the methodology and writing of the manuscript, and provided the
resources to run the experiments.

Competing interests. The authors have no competing interest.

480 *Acknowledgements.* We thank Mirjam Tijhuis and Menno Veerman for their input in discussions on radiative transfer and, along with Bart
van Stratum, for helping us get started with the atmospheric and radiative transfer simulations. WM and CvH, acknowledge funding from
the Dutch Research Council (NWO) (grant: VI.Vidi.192.068).

References

Barrett, A. I., Hogan, R. J., and Forbes, R. M.: Why are mixed-phase altocumulus clouds poorly predicted by large-scale models? Part 1. Physical processes, Journal of Geophysical Research: Atmospheres, 122, 9903–9926, https://doi.org/10.1002/2016JD026321, _eprint: https://onlinelibrary.wiley.com/doi/pdf/10.1002/2016JD026321, 2017.

Gristey, J. J., Feingold, G., Glenn, I. B., Schmidt, K. S., and Chen, H.: On the Relationship Between Shallow Cumulus Cloud Field Properties and Surface Solar Irradiance, Geophysical Research Letters, 47, e2020GL090 152, https://doi.org/10.1029/2020GL090152, _eprint: https://onlinelibrary.wiley.com/doi/pdf/10.1029/2020GL090152, 2020.

Gschwind, B., Wald, L., Blanc, P., Lefèvre, M., Schroedter-Homscheidt, M., and Arola, A.: Improving the McClear model estimating the downwelling solar radiation at ground level in cloud-free conditions – McClear-v3, metz, 28, 147–163, https://doi.org/10.1127/metz/2019/0946, 2019.

Gueymard, C. A.: Cloud and albedo enhancement impacts on solar irradiance using high-frequency measurements from thermopile and photodiode radiometers. Part 1: Impacts on global horizontal irradiance, Solar Energy, 153, 755–765, https://doi.org/10.1016/j.solener.2017.05.004, 2017.

Hogan, R. J., Fielding, M. D., Barker, H. W., Villefranque, N., and Schäfer, S. A. K.: Entrapment: An Important Mechanism to Explain the Shortwave 3D Radiative Effect of Clouds, Journal of the Atmospheric Sciences, 76, 2123–2141, https://doi.org/10.1175/JAS-D-18-0366.1, publisher: American Meteorological Society Section: Journal of the Atmospheric Sciences, 2019.

Knap, W. H. and Mol, W. B.: High resolution solar irradiance variability climatology dataset part 1: direct, diffuse, and global irradiance, https://doi.org/10.5281/zenodo.7093164, 2022.

Li, J., Huang, J., Stamnes, K., Wang, T., Lv, Q., and Jin, H.: A global survey of cloud overlap based on CALIPSO and CloudSat measurements, Atmospheric Chemistry and Physics, 15, 519–536, https://doi.org/10.5194/acp-15-519-2015, publisher: Copernicus GmbH, 2015.

Mol, W., Heusinkveld, B., and van Heerwaarden, C.: Radiometer grid at Falkenberg and surroundings, downwelling shortwave radiation, FESSTVaL campaign, https://doi.org/10.25592/uhhfdm.12548, 2023a.

Mol, W., Heusinkveld, B., Mangan, M. R., Hartogensis, O., Veerman, M., and van Heerwaarden, C.: Observed patterns of surface solar irradiance under cloudy and clear-sky conditions, Quarterly Journal of the Royal Meteorological Society, n/a, https://doi.org/10.1002/qj.4712, _eprint: https://onlinelibrary.wiley.com/doi/pdf/10.1002/qj.4712, 2024.

Mol, W. B., Knap, W. H., and van Heerwaarden, C. C.: High resolution solar irradiance variability climatology dataset part 2: classifications, supplementary data, and statistics, https://doi.org/10.5281/zenodo.7092058, 2022.

Mol, W. B., Knap, W. H., and van Heerwaarden, C. C.: Ten years of 1 Hz solar irradiance observations at Cabauw, the Netherlands, with cloud observations, variability classifications, and statistics, Earth System Science Data, 15, 2139–2151, https://doi.org/10.5194/essd-15-2139-2023, publisher: Copernicus GmbH, 2023b.

Pecenak, Z. K., Mejia, F. A., Kurtz, B., Evan, A., and Kleissl, J.: Simulating irradiance enhancement dependence on cloud optical depth and solar zenith angle, Solar Energy, 136, 675–681, https://doi.org/10.1016/j.solener.2016.07.045, 2016.

Prahl, S.: miepython: Pure python implementation of Mie scattering, https://doi.org/10.5281/zenodo.8218010, 2023.

Robinson, P. J.: Measurements of Downward Scattered Solar Radiation from Isolated Cumulus Clouds, Journal of Applied Meteorology and Climatology, 16, 620–625, https://doi.org/10.1175/1520-0450(1977)016<0620:MODSSR>2.0.CO;2, publisher: American Meteorological Society Section: Journal of Applied Meteorology and Climatology, 1977.

Schade, N. H., Macke, A., Sandmann, H., and Stick, C.: Enhanced solar global irradiance during cloudy sky conditions, Meteorologische
Zeitschrift, pp. 295–303, https://doi.org/10.1127/0941-2948/2007/0206, publisher: Schweizerbart'sche Verlagsbuchhandlung, 2007.

Schäfer, S. A. K., Hogan, R. J., Klinger, C., Chiu, J. C., and Mayer, B.: Representing 3-D cloud radiation effects in two-stream
schemes: 1. Longwave considerations and effective cloud edge length, Journal of Geophysical Research: Atmospheres, 121, 8567–8582,
https://doi.org/10.1002/2016JD024876, _eprint: https://onlinelibrary.wiley.com/doi/pdf/10.1002/2016JD024876, 2016.

Segal, M. and Davis, J.: The Impact of Deep Cumulus Reflection on the Ground-Level Global Irradiance, Journal of Applied Meteorology and
Climatology, 31, 217–222, https://doi.org/10.1175/1520-0450(1992)031<0217:TIODCR>2.0.CO;2, publisher: American Meteorological
Society Section: Journal of Applied Meteorology and Climatology, 1992.

Tijhuis, M., van Stratum, B. J. H., Veerman, M. A., and van Heerwaarden, C. C.: An Efficient Parameterization for Surface Short-
wave 3D Radiative Effects in Large-Eddy Simulations of Shallow Cumulus Clouds, Journal of Advances in Modeling Earth Systems,
15, e2022MS003 262, https://doi.org/10.1029/2022MS003262, _eprint: https://onlinelibrary.wiley.com/doi/pdf/10.1029/2022MS003262,
2023.

van Heerwaarden, C. C., van Stratum, B. J. H., Heus, T., Gibbs, J. A., Fedorovich, E., and Mellado, J. P.: MicroHH 1.0: a computational
fluid dynamics code for direct numerical simulation and large-eddy simulation of atmospheric boundary layer flows, Geoscientific Model
Development, 10, 3145–3165, https://doi.org/10.5194/gmd-10-3145-2017, publisher: Copernicus GmbH, 2017.

Veerman, M. A., van Stratum, B. J. H., and van Heerwaarden, C. C.: A case study of cumulus convection over land in cloud-resolving sim-
ulations with a coupled ray tracer, Geophysical Research Letters, n/a, e2022GL100 808, https://doi.org/10.1029/2022GL100808, _eprint:
https://onlinelibrary.wiley.com/doi/pdf/10.1029/2022GL100808, 2022.

Veerman, M. A., Pincus, R., Mlawer, E. J., and van Heerwaarden, C. C.: The Impact of Radiative Transfer at Reduced Spectral Res-
olution in Large-Eddy Simulations of Convective Clouds, Journal of Advances in Modeling Earth Systems, 16, e2023MS003 699,
https://doi.org/10.1029/2023MS003699, _eprint: https://onlinelibrary.wiley.com/doi/pdf/10.1029/2023MS003699, 2024.

Villefranque, N., Barker, H. W., Cole, J. N. S., and Qu, Z.: A Functionalized Monte Carlo 3D Radiative Transfer Model: Ra-
diative Effects of Clouds Over Reflecting Surfaces, Journal of Advances in Modeling Earth Systems, 15, e2023MS003 674,
https://doi.org/10.1029/2023MS003674, _eprint: https://onlinelibrary.wiley.com/doi/pdf/10.1029/2023MS003674, 2023.

Várnai, T. and Davies, R.: Effects of Cloud Heterogeneities on Shortwave Radiation: Comparison of Cloud-Top Vari-
ability and Internal Heterogeneity, Journal of the Atmospheric Sciences, 56, 4206–4224, https://doi.org/10.1175/1520-
0469(1999)056<4206:EOCHOS>2.0.CO;2, publisher: American Meteorological Society Section: Journal of the Atmospheric Sciences,
1999.

Weisman, M. L. and Klemp, J. B.: The Dependence of Numerically Simulated Convective Storms on Vertical Wind Shear and Buoyancy,
Monthly Weather Review, 110, 504–520, https://doi.org/10.1175/1520-0493(1982)110<0504:TDONSC>2.0.CO;2, publisher: American
Meteorological Society Section: Monthly Weather Review, 1982.

Yordanov, G. H.: A study of extreme overirradiance events for solar energy applications using NASA's I3RC Monte Carlo radiative transfer
model, Solar Energy, 122, 954–965, https://doi.org/10.1016/j.solener.2015.10.014, 2015.

Yordanov, G. H., Saetre, T. O., and Midtgård, O.-M.: Extreme overirradiance events in Norway: 1.6 suns measured close to 60°N, Solar
Energy, 115, 68–73, https://doi.org/10.1016/j.solener.2015.02.020, 2015.